Geophysical Research Letters

Supporting Information for

Evaluation of Morphodynamic Controls on the Preservation of Fluvial Meander-belt Deposits

N. Yan[1], L. Colombera[1], and N. P. Mountney[1]

[1]Fluvial, Eolian & Shallow-Marine Research Group, School of Earth and Environment, University of Leeds, Leeds, LS2 9JT, United Kingdom.

Contents of this file

Introduction

This document provides a detailed description of methodology and additional supporting figures.

Text S1. Methodology

Thirty-four modern and recent natural meander-belt examples were selected for use in this study. These examples are representative of a range of meander transformation styles, record different degrees of bend-apex rotation, and incorporate a variable number of neck or chute cutoffs (Figure S1 and Table S1). The same types of planform morphodynamic evolutions seen in these meander belts were modeled by PB-SAND in application to idealized scale-free simulations. The real-world natural examples were employed to derive channel trajectories that track the temporal evolution of the rivers. The channel trajectories for thirty examples were constrained by high resolution LiDAR elevation data (cases 1-30); for two meander-belt reaches of the Sacramento, interpretations by Greco and Alford (2003) were referred to (cases 31-32); two meander-belt segments of the Mississippi have been modeled integrating observations from satellite images with channel trajectories digitized by Wiman et al. (2021) based on paleochannels mapped originally by Fisk (1944) (cases 33-34). The chosen examples have been selected to cover a range of accretion styles and variable degrees of channel-belt maturity. All meander-belt examples have been normalized by scaling them to the same channel width, to enable comparisons of quantities that depend on river-system size in nature (namely the time recorded by a channel-belt of a given extent). The modeling outputs are then applied to compare how preservation of meander-belt deposits varies over different temporal and spatial scales, for different hierarchies of sedimentary products (from smaller-scale pairs of accretion packages, to sets of multiple depositional packages associated with a state of meander transformation, to larger-scale channel belts).

The Point-Bar Sedimentary Architecture Numerical Deduction, PB-SAND (Yan et al., 2017), is used to model the planform evolution seen in the chosen meander belts based on the channel trajectories defined for each example. Additional centerlines that represent the planform expression of accretion surfaces, and which reflect the position of the river course between the input trajectories, are generated by linear interpolation. The number of accretion packages between two input trajectories were specified based on the planform spacing of scroll-bar morphologies observed in high-resolution LiDAR images. The average spacing across all the models (0.18 times channel widths) is consistent with that reported in the literature for the Mississippi River (Strick et al., 2018) (Figure S2). Meander-belt accretion is simulated in steps during which both erosion and deposition of accretion packages can take place, whereas no erosion is modeled within each accretion package bounded by two consecutive accretions surfaces. Although PB-SAND can be applied to model the 3D sedimentary architecture and facies distributions of meander belts and their accumulated deposits arising from different morphodynamics processes (Yan et al., 2017, 2020), in view of the scope of this research, only 2D planform evolutions of meander belts are reconstructed in this work.

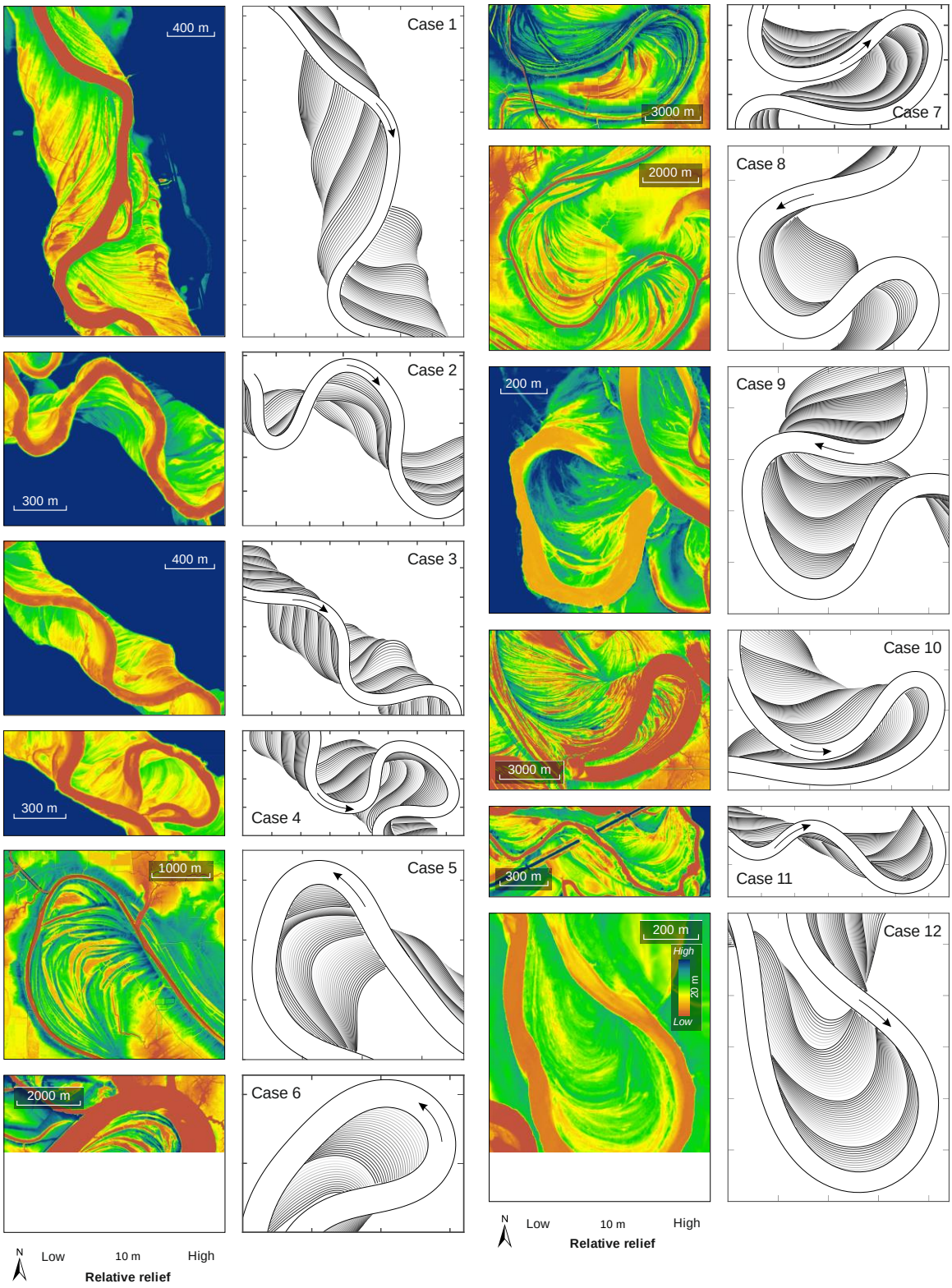

Figure S1. Thirty-four meander-belt cases portraying the planforms modeled using PB-SAND and corresponding model outputs. Arrows show flow direction.

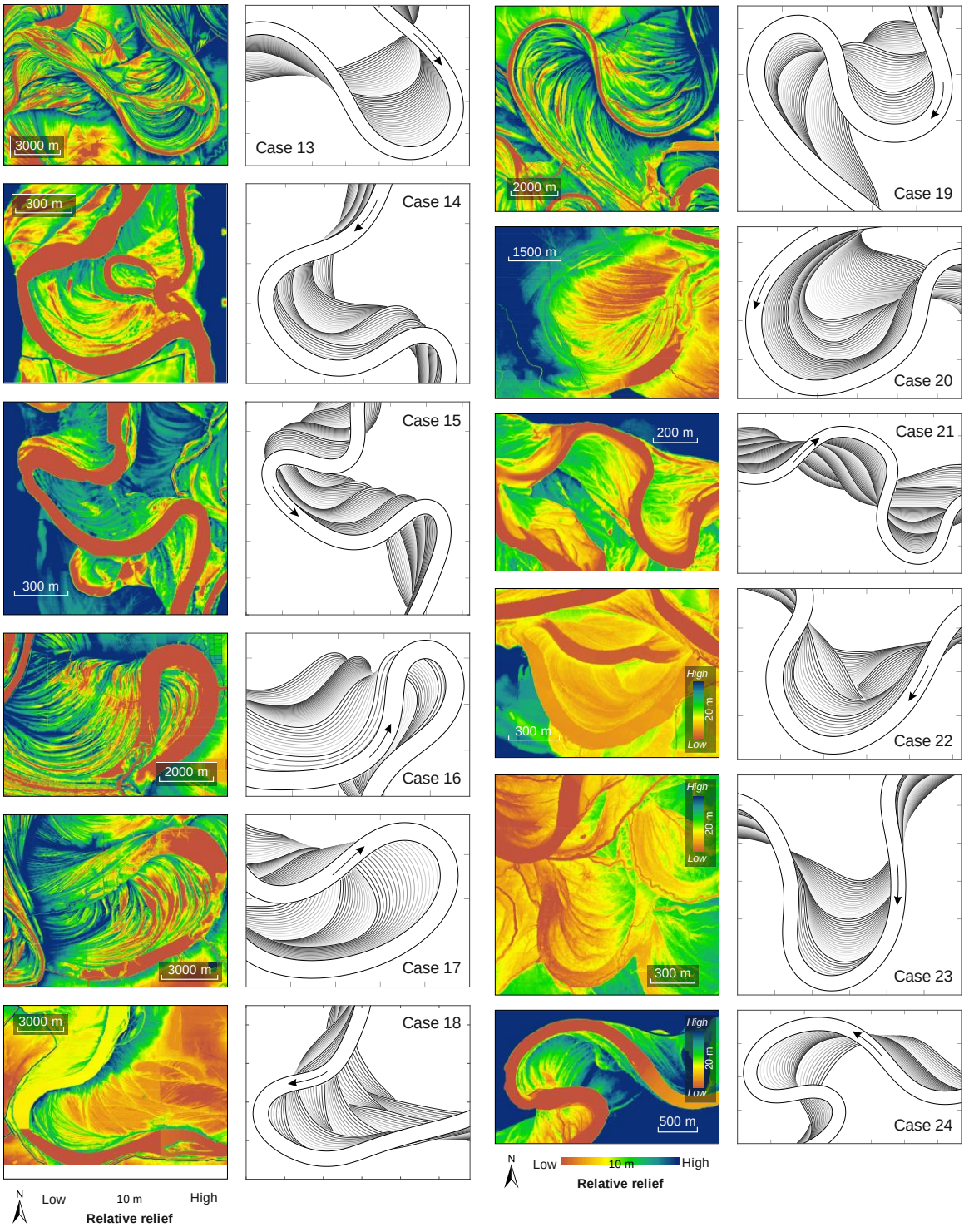

Figure S1. Continued.

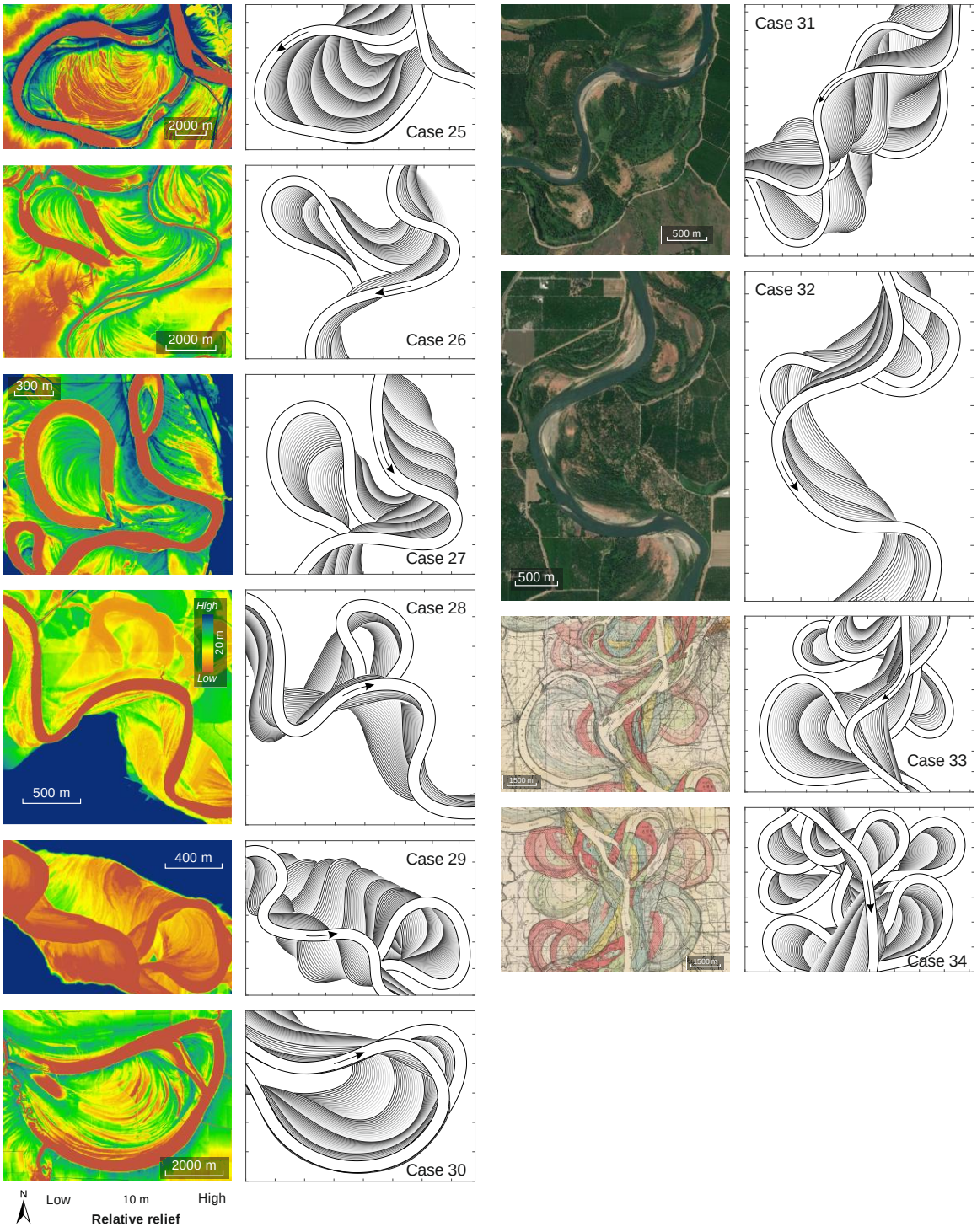

Figure S1. Continued.

Planform ID	Coordinates		Location
1	119° 24' 56'' W	48° 50' 00'' N	Okanogan, USA
2	29° 28' 07'' E	66° 20' 37'' N	Oulanka, Finland
3	29° 33' 21'' E	66° 18' 45'' N	Oulanka, Finland
4	29° 30' 36'' E	66° 19' 54'' N	Oulanka, Finland
5	119° 25' 11'' W	48° 51' 31'' N	Okanogan, USA
6	91° 32' 36'' W	31° 53' 57'' N	Mississippi, USA
7	91° 53' 16'' W	30° 48' 53'' N	Mississippi, USA
8	91° 21' 29'' W	32° 18' 37'' N	Mississippi, USA
9	119° 42' 43'' W	48° 57' 43'' N	Okanogan, USA
10	91° 32' 18'' W	31° 46' 13'' N	Mississippi, USA
11	119° 39' 24'' W	48° 55' 40'' N	Okanogan, USA
12	120° 06' 00'' W	46° 15' 34'' N	Yakima, USA
13	91° 27' 19'' W	31° 51' 10'' N	Mississippi, USA
14	91° 30' 06'' W	30° 46' 21'' N	Mississippi, USA
15	119° 26' 15'' W	48° 54' 30'' N	Okanogan, USA
16	91° 44' 45'' W	31° 29' 31'' N	Mississippi, USA
17	91° 38' 19'' W	31° 38' 40'' N	Mississippi, USA
18	120° 03' 53'' W	46° 14' 42'' N	Yakima, USA
19	91° 21' 50'' W	32° 03' 30'' N	Mississippi, USA
20	92° 02' 39'' W	30° 55' 20'' N	Mississippi, USA
21	119° 40' 28'' W	48° 56' 47'' N	Okanogan, USA
22	91° 36' 46'' W	31° 33' 43'' N	Mississippi, USA
23	121° 34' 19'' W	48° 28' 42'' N	Skagit, USA
24	121° 50' 24'' W	48° 32' 05'' N	Skagit, USA
25	91° 25' 20'' W	30° 38' 50'' N	Mississippi, USA
26	91° 22' 25'' W	32° 21' 27'' N	Mississippi, USA
27	119° 25' 13'' W	48° 51' 33'' N	Okanogan, USA
28	120° 04' 05'' W	46° 14' 56'' N	Yakima, USA
29	29° 35' 10'' E	66° 18' 21'' N	Oulanka, Finland
30	91° 13' 34'' W	32° 27' 29'' N	Mississippi, USA
31	121° 57' 42" W	39° 40' 55" N	Sacramento, USA
32	122° 00' 03" W	39° 30' 54" N	Sacramento, USA
33	91° 08' 46" W	33° 20' 26" N	Mississippi, USA
34	91° 05' 41" W	33° 13' 01" N	Mississippi, USA

Table S1. Location of thirty-four real-world meander-belt examples that display the same channel evolutions of the idealized models simulated in this work.

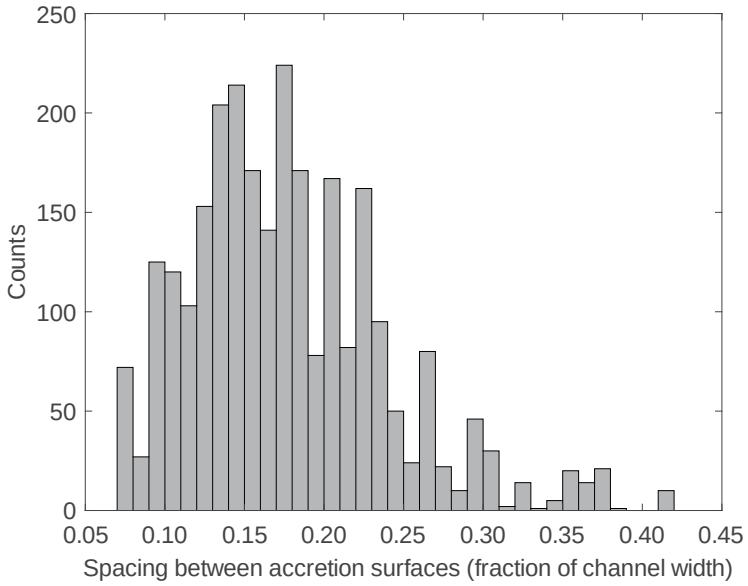

Figure S2. Distribution of the maximum spacing between accretion surfaces normalized by the channel width, from all 34 cases.

The 'preservation ratio' is the fraction of meander-belt deposits that are preserved over a given timescale, and is quantified as the ratio between the planform area covered by deposits accumulated over a certain length of time that are preserved at the end of that time window (area of net deposition) and the area over which the river has wandered over the same length of time (area of river migration) (Durkin et al., 2018). The preservation ratio is separately calculated for three hierarchies of architectural products:

(i) pairs of accretion packages, whereby each package is contained between two consecutive accretion surfaces. Accretion packages can be regarded as analogous to flood-interflood units; however, they are modelled to have developed at a constant rhythm because accretion is simulated through linear interpolation between two input trajectories. Erosion within individual accretion packages is not simulated.

(ii) sets of accretion packages bounded by two consecutive input trajectories, which represent portions of channel belts undergoing a certain style of meander transformations and are here termed 'stages' (stages contain between 5 and 40 accretion packages, 16 on average).

(iii) meander-belt segments that are composed of multiple sets of accretion packages, each of which may be dominated by different styles of meander

transformations, and that record a variable number of bend cut-offs (from 0 to 6).

The time recorded in each accretion package is determined by the ratio between channel migration distance and channel migration rate. The channel migration distance was determined by the ratio of the area of river migration of each package to the average channel length of the two channel centerlines that define the package. The channel migration distance was then normalized with the channel width (arbitrary and of the same size across the 34 examples), as the 'normalized migration distance'. Values of average channel migration rate over each depositional package enclosed by two channel centerlines was determined based on three alternative assumptions of its relationship with the channel radius of curvature (Howard and Knutson, 1984; Hudson and Kesel, 2000; Nanson and Hickin, 1983; Sylvester et al., 2019). Three relationships between the normalized migration rate and the channel radius of curvature are considered, which yield three separate proxies for the temporal scale of river evolution: (i) channel migration rate remains constant for any value of channel radius of curvature; (ii) migration rate increases monotonically as the channel radius of curvature decreases (i.e. channel curvature increases); (iii) migration rate increases as the channel radius of curvature decreases towards 2.44 (cf. Howard and Knutson, 1984), and then decreases with increasing channel curvature (decreasing radius) for smaller radii of curvature. The second and third alternatives are determined based on relationships between channel radius of curvature and nominal migration rates that returned realistic relationships between actual channel migration rates and channel curvature in models by Howard and Knutson (1984, Figure 1a). The two relationships are presented in Figure 1d, in which the dimensionless arbitrary scale of Howard and Knutson (1984) is maintained. These relationships were not applied to extract migration rates for each node of a channel centerline (cf. Howard and Knutson, 1984), since each centerline represents a time step, wherefore relative rates of migration along each are given by the offset of these nodes relative to correlative nodes in neighboring centerline; instead, the relationships were used to extract dimensionless average migration rates for each package based on the average radius of curvature of two channel centerlines enclosing a sedimentary package. Across the entire set of channel trajectories (N = 3,952), the median value of the average radius of curvature of the centerlines is similar to the median of the local radii of curvature at the centerline nodes ('control points', Figure S3), and the two distributions are similarly skewed. The accretion time (t, dimensionless) was determined as the ratio of the normalized migration distance to the average migration rate:

$$\boldsymbol{t} = \left(\frac{\boldsymbol{A}}{\boldsymbol{LW}}\right) / \boldsymbol{M}$$

where A is the surface area of deposited package enclosed by two centerlines; L is the average length of two channel centerlines of a meander-belt segment; W is the channel width; M is the dimensionless average migration rate of the channel. M is equal to 1 for the first alternative, for which channel migration rate does not change with the average channel radius of curvature: in this case the migration distance is taken as a direct proxy

for time. The two time proxies associated with the second and third alternatives are also employed to compute meander-belt accretion rates for different hierarchies of architectural products: these accretion rates are defined as the ratios between preserved accretion distance divided by the time proxies.

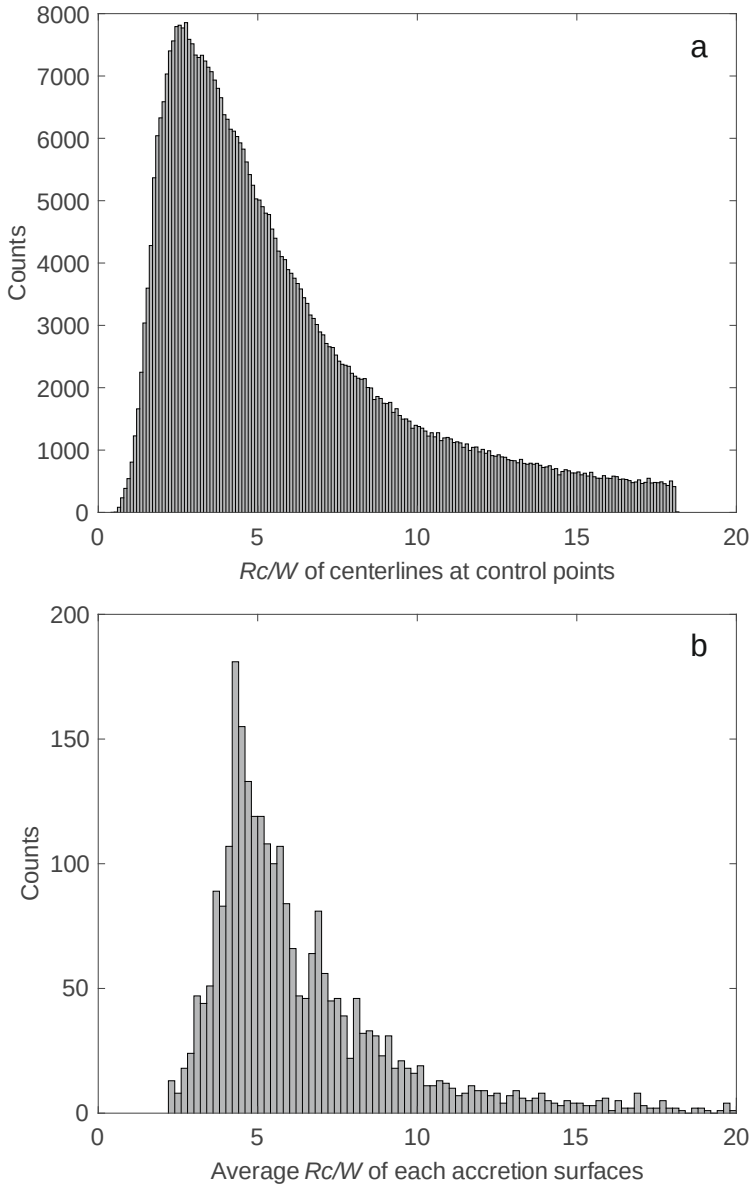

Figure S3. Distribution of the radius curvature of control points (A) and the average radius curvature of each accretion surface (B), both of which are normalized by the channel width, from all 34 cases.

Planform characteristics of each hierarchy of architectural products were analyzed including mean sinuosity, meander rotation, circular variance of channel orientation, and migration angle (Figure S4). The channel sinuosity is calculated as the ratio between the streamwise length and the straight distance between the two end points of each

modeled channel trajectory (Friend and Sinha, 1993). The channel sinuosity is further characterized by the circular variance of channel orientation, based on the downstream direction of pairs of consecutive control points (vector nodes) along the channel centerline. The degree of rotation of each meander is defined as the change of direction of the meander apex (itself identified as the point of local maximum curvature between two channel inflection points) across two consecutive accretion packages. The migration angle of each accretion package is defined as the absolute angle between the direction of channel migration, approximated by the direction of shift of corresponding control points across two consecutive trajectories, and the circular mean of downstream channel direction used as an approximation of the channel-belt orientation.

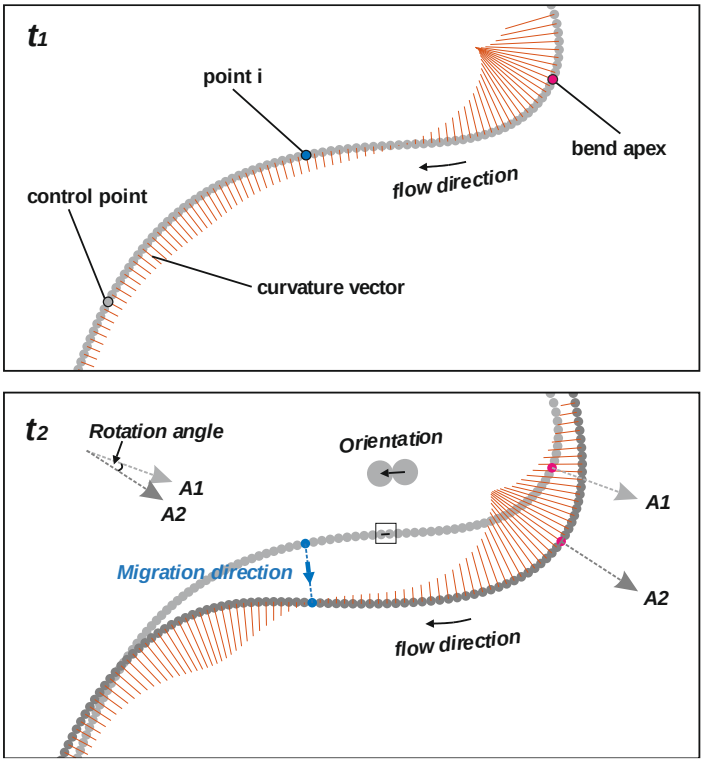

Figure S4. Schematic diagram showing how quantitative parameters of point-bar planform evolution are defined. Control points (vector nodes) of two consecutive channel centerlines at t1 and t2 are shown as gray spots. Each centerline has the same number of control points. The migration direction is calculated by the shift of each control point across consecutive centerlines. The channel orientation is estimated as a downstream-oriented vector connecting two consecutive control points along each centerline. The red lines denote the curvature vector of each control point, whereby a greater length indicates a sharper bend. The degree of apex rotation is the change in

migration direction seen between consecutive centerlines at the point of local maximum bend curvature (from Yan et al., 2020).

Limitations

The proposed approach is subject to several limitations. The assessment of sediment preservation of meander belts was undertaken considering planform areas as proxies for sediment volumes (Durkin et al., 2018). These volumetric estimations do not account for changes in meander-belt thickness in relation to streamwise variations in channel bathymetry (e.g., across meander pools and riffle zones, Yan et al., 2020). Furthermore, preservation of the lowermost portion of point-bar deposits caused by streambed aggradation is ignored in this particular study. Other possible limitations exist that are associated with necessary simplifications of the modeling approach. For example, the time embodied by accretion packages was calculated based on trajectories that are linearly interpolated so as to obtain accretion patterns that match with a realistic scroll-bar spacing (Strick et al., 2018); however, the spacing of scroll bars on point-bar surfaces may not accurately reflect the tempo of point-bar accretion, particularly in situations where erosional processes occur to shape scroll-bar morphologies (Mason and Mohrig, 2019; Nanson and Hickin, 1983). Another important simplification is made by computing the surface areas of accretion packages based on the migration of channel centerlines, rather than channel thalwegs, hence disregarding the fact that thalwegs will typically be offset relative to the centerlines, especially at pools located at meander apices. Examples of amalgamated meander-belt examples recording multiple episodes of neck or chute cutoffs, which cover the largest temporal scales considered, were modeled based on channel trajectories that are partly extracted from historical maps, which have lower temporal resolution than remote-sensing datasets.

References

Durkin, P. R., Hubbard, S. M., Holbrook, J., & Boyd, R. (2018). Evolution of fluvial meander-belt deposits and implications for the completeness of the stratigraphic record. *GSA Bulletin, 130*(5-6), 721-739. https://doi.org/10.1130/B31699.1

Fisk, H. N. (1944). *Geological investigation of the alluvial valley of the lower Mississippi River*. U.S. Department of the Army, Mississippi River Commission.

Friend, P. F., & Sinha, R. (1993). Braiding and meandering parameters. In J. R. Best, & C. S. Bristow (Eds.), *Braided Rivers, Geological Society, London, Special Publications 75*, 105-111. m

Hudson, P. F., & Kesel, R. H. (2000). Channel migration and meander-bend curvature in the lower Mississippi River prior to major human modification. *Geology, 28*(6), 531-534. https://doi.org/10.1130/0091-7613(2000)28<531:CMAMCI>2.0.CO;2

Mason, J., & Mohrig, D. (2019). Scroll bars are inner bank levees along meandering river bends. *Earth Surface Processes and Landforms, 44*(13), 2649-2659. https://doi.org/10.1002/esp.4690

Nanson, G. C., & Hickin, E. J. (1983). Channel Migration and Incision on the Beatton River. *Journal of Hydraulic Engineering, 109*(3), 327-337. https://doi.org/10.1061/(ASCE)0733-9429(1983)109:3(327)

Strick, R. J. P., Ashworth, P. J., Awcock, G., & Lewin, J. (2018). Morphology and spacing of river meander scrolls. *Geomorphology, 310,* 57-68. https://doi.org/10.1016/j.geomorph.2018.03.005

Sylvester, Z., Durkin, P., & Covault, J. A. (2019). High curvatures drive river meandering. *Geology, 47*(3), 263-266. https://doi.org/10.1130/G45608.1

Wiman, C., Hamilton, B., Dee, S. G., & Muñoz, S. E. (2021). Reduced lower Mississippi River discharge during the Medieval era. *Geophysical Research Letters, 48*(3), e2020GL091182. https://doi.org/10.1029/2020GL091182

Yan, N., Colombera, L., & Mountney, N. P. (2020). Controls on fluvial meander-belt thickness and sand distribution: Insights from forward stratigraphic modelling. *Sedimentology*. https://doi.org/10.1111/sed.12830

Yan, N., Mountney, N. P., Colombera, L., & Dorrell, R. M. (2017). A 3D forward stratigraphic model of fluvial meander-bend evolution for prediction of point-bar lithofacies architecture. *Computers & Geosciences, 105,* 65-80. https://doi.org/10.1016/j.cageo.2017.04.012

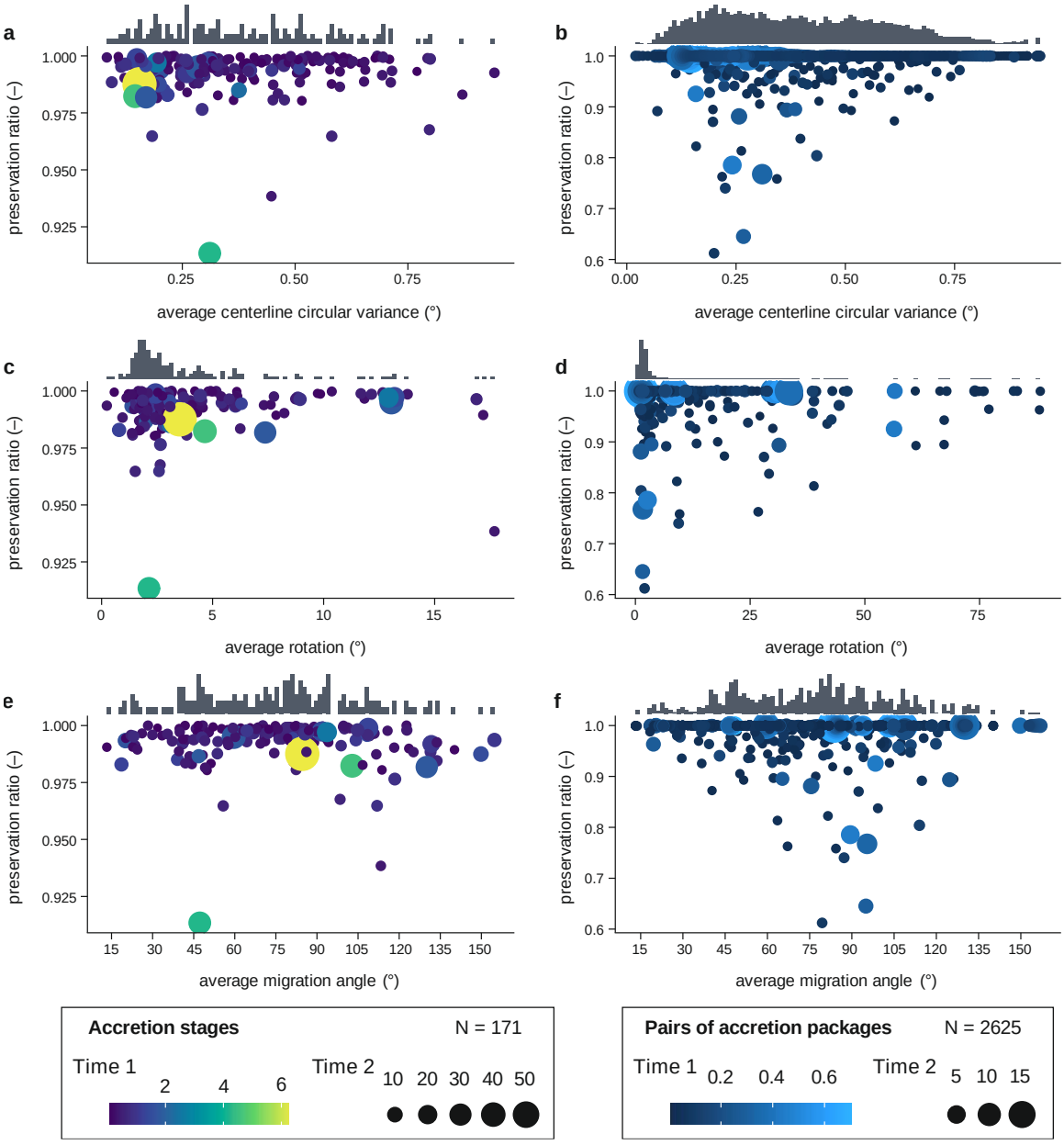

Figure S5. Relationships between the preservation ratio, planform characteristics and timescale of accretion stages and pairs of accretion packages, and associated distributions of planform metrics. The scatterplots show relationships between: average centerline circular variance and preservation ratio, for accretion stages (A) and pairs of packages (B); average meander-bend rotation and preservation ratio, for accretion stages (C) and pairs of packages (D); average migration angle (dominant accretion direction relative to channel orientation) and preservation ratio, for accretion stages (E) and pairs of packages (F).